Available online at www.sciencedirect.com
ScienceDirect
Trans. Nonferrous Met. Soc. China 34(2024) 1951−1964
Transactions of Nonferrous Metals Society of China
www.tnmsc.cn

Performance and mechanism of constructed CuO/CeO_2 p–n heterojunction for photocatalytic degradation of methylene blue

Huan-huan CHEN[1,2], Shao-hua LUO[1,2], Xue-fei LEI[1,2], Fei TENG[1,2], Xian-bing JI[3], Xiao-dong LI[1]

1. School of Materials Science and Engineering, Northeastern University, Shenyang 110819, China;
2. Key Laboratory of Dielectric and Electrolyte Functional Materials of Hebei Province, Northeastern University at Qinhuangdao, Qinhuangdao 066004, China;
3. Department of Environmental Engineering, Hebei University of Environmental Engineering, Qinhuangdao 066102, China

Received 22 November 2022; accepted 9 July 2023

Abstract: CuO/CeO_2 p–n heterojunction composites were synthesized using an easy microwave reflux method with homogeneous precipitation technology, and their photocatalytic performance in terms of methylene blue degradation was studied. The results showed that the degradation effect of the CuO/CeO_2 heterojunction composites was substantially stronger than that of CeO_2. The composite prepared with a Cu/Ce molar ratio of 1/3 (1/3 Cu/Ce) exhibited the highest catalytic activity, achieving a degradation efficiency of 96.2% within 180 min. The improved photocatalytic performance was attributed to the formation of a p–n heterojunction between CuO and CeO_2, which considerably promoted the separation and transport of photogenerated carriers. The band offset of the CuO/CeO_2 heterostructure was calculated; its valence band offset was 1.58 eV and conduction band offset was −0.48 eV, further demonstrating the formation of a p–n heterojunction.

Key words: CuO; CeO_2; p–n heterojunction; photocatalytic mechanism; methylene blue

1 Introduction

Various organic wastewaters are released into the water environment, considerably affecting the ecological balance of nature and human health [1−4]. Ecofriendly, low-cost, and high-efficiency technologies must be developed for water decontamination [5−7]. Semiconductor photocatalysts can mineralize organic pollutants by producing reactive radicals; they exhibit considerable potential for decomposing various types of pollutants [8,9]. The rare earth oxide CeO_2 has high chemical corrosion resistance, light corrosion resistance, and intense ultraviolet light absorption ability. CeO_2 has a redox cycle of Ce^{3+}/Ce^{4+} and hence is widely used for the photocatalytic treatment of organic wastewater [10−12]. CeO_2 has a wide bandgap and high photogenerated carrier recombination efficiency, limiting its photocatalytic performance. To overcome this limitation, a p–n heterojunction can be constructed to reduce the bandgap and inhibit electron–hole recombination [13,14]. At the p–n heterojunction, the Fermi level can reach equilibrium through the diffusion of electrons from the n-type semiconductor to the p-type semiconductor via the interface, forming a built-in electric field pointing from the n-type semiconductor to the p-type semiconductor [15−17]. In other words, there are two driving forces for the photogenerated electron migration in p–n heterojunction: the band potential

Corresponding author: Shao-hua LUO, Tel: +86-335-8047760, E-mail: tianyanglsh@163.com;
Xue-fei LEI, Tel: +86-335-8047521, E-mail: leixf@neuq.edu.cn
DOI: 10.1016/S1003-6326(24)66518-0

difference and the built-in electric field. Therefore, p–n heterojunctions can realize the effective separation of electron–hole pairs, accelerate the charge transfer to the catalyst surface, and prolong the lifetime of the photogenerated carriers. Currently, various p–n heterojunction photocatalysts with matching-energy-level structures have been prepared [18−20], such as CeO_2/Co_3O_4 [21], NiO/CeO_2 [22], and CeO_2/CuS [23]. Although some progress has been made in this regard, there is still a need to develop CeO_2-based heterojunction photocatalysts that can effectively reduce their bandgaps and improve the charge separation efficiency of electron–hole pairs. Moreover, more research needs to be conducted on the principle of p–n heterojunction formation.

To regulate the bandgap and improve the electron–hole separation efficiency, a p-type semiconductor with a suitable bandgap can be used to compound with CeO_2 and construct a new p–n heterojunction material. As a p-type semiconductor material, CuO exhibits good visible-light absorption capacity and stable physicochemical properties and is inexpensive. Moreover, it is often compounded and modified with wide-bandgap semiconductors, thereby improving the light absorption capacity of the composite materials and separation efficiency of electron–hole pairs. BHARATHI et al [24] synthesized CuO/ZnO nanocomposites having various copper and zinc contents. Compared with ZnO, the degradation rate of methylene blue (MB) using the CuO/ZnO nanocomposites with 5% Cu content reached 96.57% within 25 min. The enhanced photocatalytic performance of the nanocomposites was attributed to the inhibition of electron–hole pair recombination due to the presence of a p–n interface. DURSUN et al [25] prepared WO_3/CuO heterojunction materials. Compared with pure WO_3, the adsorption rate and degradation speed of MB dye using the prepared sample with a CuO mass fraction of 0.75% increased by 38.4% and 25.7%, respectively. The enhanced photocatalytic activity was attributed to the formation of a heterojunction mechanism between CuO and WO_3, which promoted the photo-induced carrier separation. Recombining CeO_2 with CuO to form a p–n heterojunction will effectively improve the photocatalytic activity of CeO_2 because CeO_2 and CuO have matching band structures.

Herein, a new p–n heterostructure composite CuO/CeO_2 was prepared using an atmospheric microwave reflux method with homogeneous precipitation technology, and the effect of the CuO content on the structural, optical, and photocatalytic properties of CeO_2 was investigated. Moreover, the photocatalytic performance of CuO/CeO_2 was evaluated via the degradation of an MB solution as the model pollutant. The possible mechanism of CuO/CeO_2 p–n heterojunction for the enhanced photocatalytic activity was deduced from the results of a free-radical-trapping experiment. Furthermore, this was confirmed by calculating the shift of the band position of CuO/CeO_2 heterojunction. This method might provide a new approach for revealing the photocatalytic mechanism of p–n heterojunction composites.

2 Experimental

2.1 Preparation of CuO/CeO_2 composites

The CuO/CeO_2 composites were synthesized using a facile microwave reflux method with homogeneous precipitation technology. Briefly, 10 mmol $Ce(NO_3)_3·6H_2O$, 5 mmol $Cu(NO_3)_2·6H_2O$, 2 g polyvinylpyrrolidone and 60 mmol urea were dissolved in 100 mL deionized water and stirred to form a transparent solution. The solution was transferred to a 250 mL flask to perform a microwave reflux reaction. After microwave treatment for 60 min, a considerable precipitate was generated. The precipitate was separated via centrifugation, washed several times with distilled water and ethanol, and dried at 60 °C for 12 h. Finally, the products were calcined at 500 °C for 2 h in a muffle furnace to obtain the 1/2 Cu/Ce sample. Other CuO/CeO_2 composites were prepared by changing the molar ratio of Cu/Ce to 1/3, 1/4, and 1/6, which were then labeled as 1/3 Cu/Ce, 1/4 Cu/Ce, and 1/6 Cu/Ce, respectively.

2.2 Characterization

The phase structure of the CuO/CeO_2 composites was analyzed via X-ray diffraction (XRD) using an X-ray diffractometer (Rigaku SmartLab) with Cu K_α radiation (λ=1.541874 Å). The particle morphology and microstructure of the samples were characterized using scanning electron microscopy (SEM; Zeiss SUPRA−55) and high-resolution transmission electron microscopy

(HRTEM; Philips-FEI Tecnai F30). The specific surface area of the samples was measured using Brunauer–Emmett–Teller (BET; SSA−4300) method. Fluorescence spectra were measured using a fluorescence spectrophotometer (Hitachi F−7000). The diffuse reflectance spectra of the products were obtained using an ultraviolet–visible (UV–Vis) spectrophotometer equipped with an integration sphere (Perkin Elmer Lambda 750 s). The chemical state and elemental composition of the synthesized CuO/CeO_2 composites were determined using X-ray photoelectron spectroscopy (XPS; ESCALAB 250XI). All binding energies were calculated with reference to the energy of the C 1s peak of contaminant carbon at 284.8 eV.

2.3 Photocatalytic experiment

The photocatalytic properties of the as-prepared samples were determined via the degradation of the MB solution under UV irradiation using a 500 W mercury lamp. Briefly, a photocatalyst (150 mg) was dispersed in the MB solution (300 mL; 10 mg/L). Before irradiation, the suspension was stirred in a dark environment for 30 min to ensure adsorption–desorption equilibrium. After irradiation, 4 mL of the suspension was withdrawn every 30 min and centrifuged to remove the CuO/CeO_2 composites. Subsequently, the absorbance of the MB solution was measured at 664 nm using a UV−Vis spectrophotometer. The degradation efficiency was evaluated using the function $A_t/A_0\times100\%$, where A_0 represents the absorbance of MB after dark adsorption and A_t represents the absorbance at the illumination time t. The trapping experiments were performed using a procedure similar to the aforementioned procedure, except for the addition of tert-butyl alcohol (TBA, a hydroxyl radical scavenger), ethylenediamine tetraacetic acid disodium salt (EDTA-2Na, a hole scavenger), and *p*-benzoquinone (BQ, a superoxide radical scavenger).

3 Results and discussion

3.1 Phase composition and morphology

Figure 1 shows the XRD patterns of pure CeO_2 and CuO/CeO_2 composites. The characteristic XRD peaks indicated that the obtained CeO_2 and CuO/CeO_2 composites were well crystallized. The XRD peaks at 2θ values of 28.5°, 33.1°, 47.5°, 56.4° and 59.1° marked by the plum blossom shape were respectively indexed to (111), (200), (220), (311), and (222) crystal faces of cubic fluorite-structured CeO_2 (JCPDS No. 34-0394) [26], while XRD peaks at 2θ of 35.5° and 38.7° labeled by the rhomboid shape were assigned to the monoclinic-structured CuO [27]. For the 1/4 Cu/Ce and 1/6 Cu/Ce samples, the XRD peak corresponding to the CuO phase was absent because the amount of doped Cu was relatively low. Cu species were doped into the CeO_2 lattice in the form of ions or dispersed on the surface of CeO_2 in the form of fine CuO clusters without changing the phase structure of CeO_2 [28]. Similar phenomena have been previously reported [29]. AVGOUROPOULOS et al [30] reported that the absence of the CuO peak in CeO_2/CuO (CuO molar fraction of 15%) samples was attributed to the solid solution formed via the addition of Cu^{2+} to the CeO_2 lattice. When the Cu content was increased, two prominent XRD peaks corresponding to the CuO phase appeared in the 1/2 Cu/Ce and 1/3 Cu/Ce samples, indicating that Cu ions entering the lattice of CeO_2 reached saturation. The excessive Cu ions precipitated into the CuO phase, and the intensity of the corresponding XRD peaks gradually increased with increasing CuO content [31]. The inset in Fig. 1 shows that the XRD peak corresponding to the (111) crystal plane of the CuO/CeO_2 composite moved toward, a large angle compared with that of pure CeO_2, suggesting that the CeO_2 lattice was doped with Cu ions. Additionally, the XPS survey spectrum for 1/3 Cu/Ce revealed that the composites comprised Cu, Ce, and O.

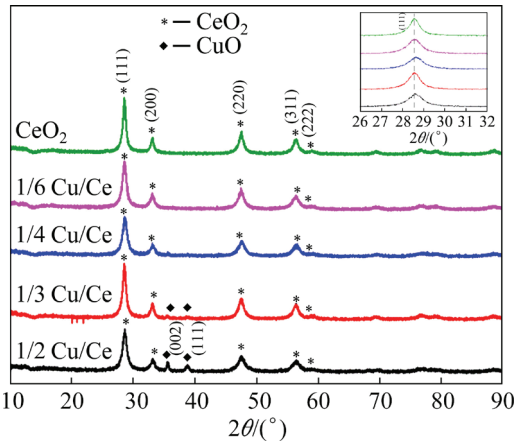

Fig. 1 XRD patterns for pure CeO_2 and CuO/CeO_2 composites

Figure 2 presents typical SEM images of pure CeO_2 and CuO/CeO_2 composites. The pure CeO_2 prepared using the microwave reflux method presents regular rhombohedra-shaped morphologies. Interestingly, as CuO and CeO_2 were compounded, the morphology of CeO_2 in CuO/CeO_2 composites completely changed from rhombohedra shape to polyhedral shape, whereas CuO exhibited a regular spherical shape and was dispersed around or on the surface of the polyhedrons. The well-dispersed CuO and CeO_2 exhibited a strong interfacial interaction, promoting the transfer of photogenerated carriers on the surface of the CuO/CeO_2 composites, which is conducive to improving their photocatalytic activity. Furthermore, the number of CuO spheres increased with increasing Cu/Ce molar ratio, which is consistent with the increasing trend of the intensity of the CuO peak in the XRD pattern.

Transmission electron microscopy (TEM) images of 1/3 Ce/Cu were obtained for a closer examination of the microstructure of 1/3 Ce/Cu. Figure 3(a) presents the TEM image of 1/3 Ce/Cu. As shown in this figure, 1/3 Ce/Cu exhibited two morphologies: spherical particles and polyhedral structures. The CuO spheres were attached to the surface of CeO_2 polyhedron to form an intimate interfacial contact, which can be observed in the TEM image. The lattice fringes are visible in the HRTEM image shown in Fig. 3(b), with interplanar spacings of 0.19 and 0.23 nm corresponding to the (220) plane of CeO_2 and (111) plane of CuO, respectively.

Figure 4 shows the N_2 adsorption–desorption isotherms and pore size distribution of pure CeO_2 and CuO/CeO_2 composites. The prepared nanoparticles presented a type-IV isotherm curve with a H4 hysteresis loop based on the IUPAC classification [32], reflecting the presence of mesopores in the sample. Furthermore, stacking of the samples led to the formation of pores. Except

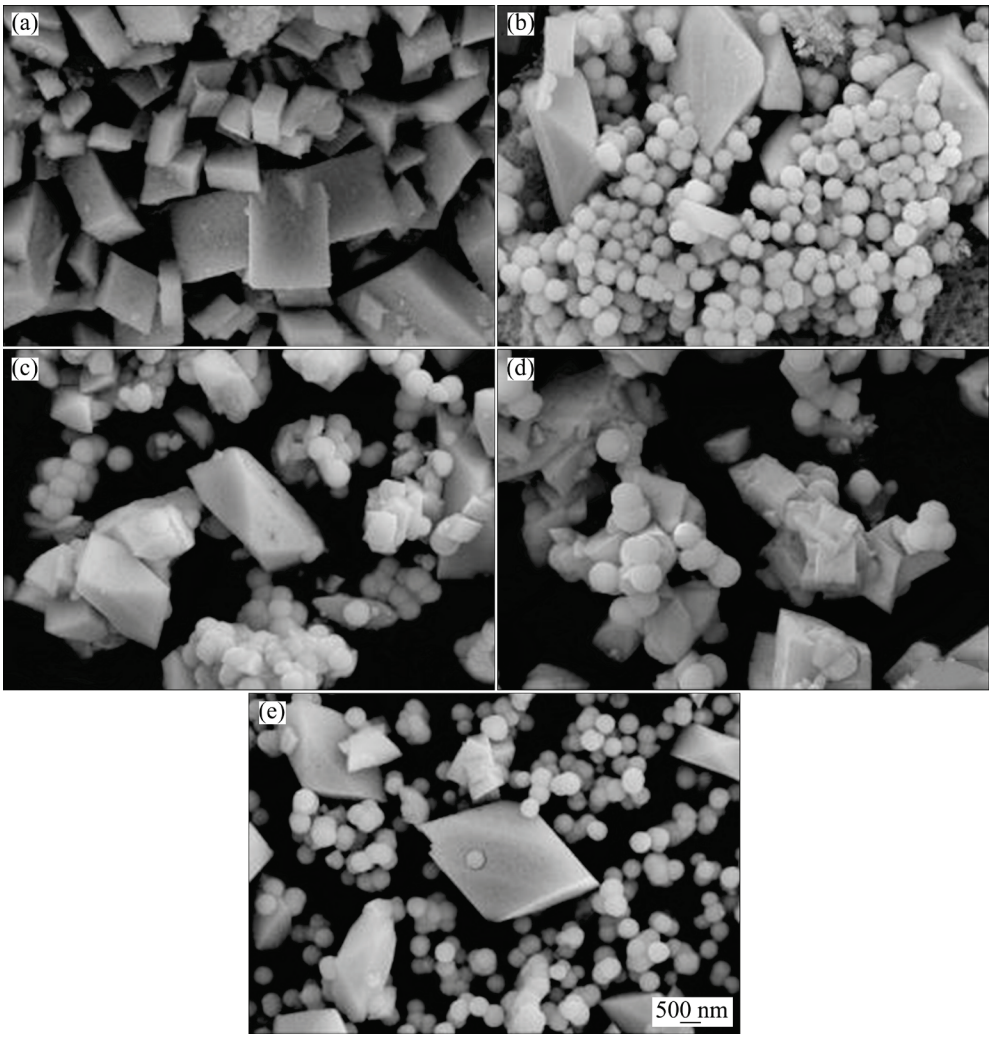

Fig. 2 SEM images of pure CeO_2 (a), 1/2 Cu/Ce (b), 1/3 Cu/Ce (c), 1/4 Cu/Ce (d) and 1/6 Cu/Ce (e)

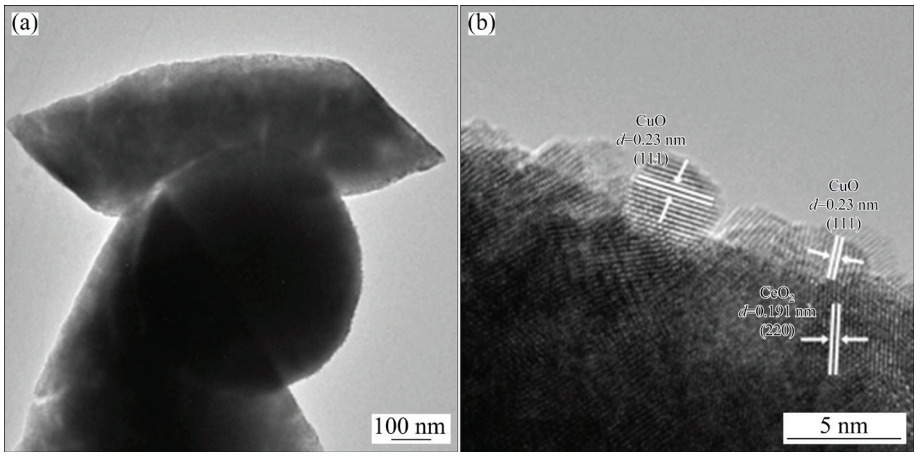

Fig. 3 TEM (a) and HRTEM (b) images of 1/3 Cu/Ce

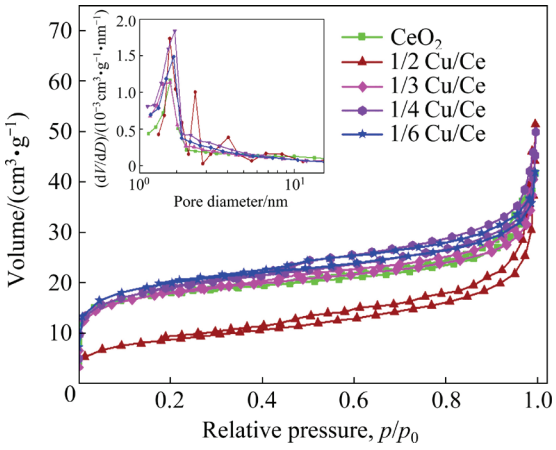

Fig. 4 N_2 adsorption−desorption isotherms and pore size distribution curves (inset) for pure CeO_2 and CuO/CeO_2 composites

for the 1/2 Cu/Ce samples, incorporating CuO increased the specific surface area of the CuO/CeO_2 composites. The BET surface area of the CuO/CeO_2 composites gradually decreased with increasing CuO content, suggesting that adding excessive CuO is not conducive to increasing the specific surface area of the samples. The surface area of the samples decreased with increasing CuO content, which is in accordance with a previous report [33].

The average pore size distribution of CuO/CeO_2 composites measured using the Barrett–Joyner–Halenda method was 2−10 nm, which is in the mesoporous range and consistent with the adsorption–desorption isotherm results (Fig. 4). Table 1 lists the pore volume, BET surface area, and average pore size of the samples. The specific surface area of 1/3 Cu/Ce (62.3 m^2/g) is slightly smaller than those of 1/4 Cu/Ce and 1/6 Cu/Ce (64.5 and 66.1 m^2/g, respectively). This indicates that the specific surface area of the CuO/CeO_2 composite does not considerably increase with the combination of CuO and CeO_2.

Table 1 Specific surface area, pore volume and pore radius of CeO_2 and CuO/CeO_2 composites

Sample	Specific surface area/($m^2 \cdot g^{-1}$)	Pore volume/($cm^3 \cdot g^{-1}$)	Average pore radius/nm
CeO_2	56.2	0.042	6.41
1/2 Cu/Ce	30.7	0.073	8.60
1/3 Cu/Ce	62.3	0.041	5.22
1/4 Cu/Ce	64.5	0.057	5.21
1/6 Cu/Ce	66.1	0.041	4.67

3.2 Diffuse reflectance spectroscopy (DRS), photoluminescence (PL), and XPS results

Generally, the performance of photocatalysts strongly depends on their optical activities. Therefore, the optical absorption performance of pure CeO_2 and CuO/CeO_2 composites was investigated using UV–Vis DRS. As shown in Fig. 5(a), pure CeO_2 exhibited a strong absorption band at a wavelength < 400 nm, which is consistent with previous studies [34]. In contrast to pure CeO_2, all the CuO/CeO_2 composites exhibited strong responses to UV and visible light. After introducing CuO, the absorption intensity of the CuO/CeO_2 composites considerably increased in the wavelength range of 400−800 nm and the absorption edge was slightly red-shifted. This suggests that CuO/CeO_2 composites exhibit better light absorption performance and photocatalytic activity than pure CeO_2. This may be because the combination

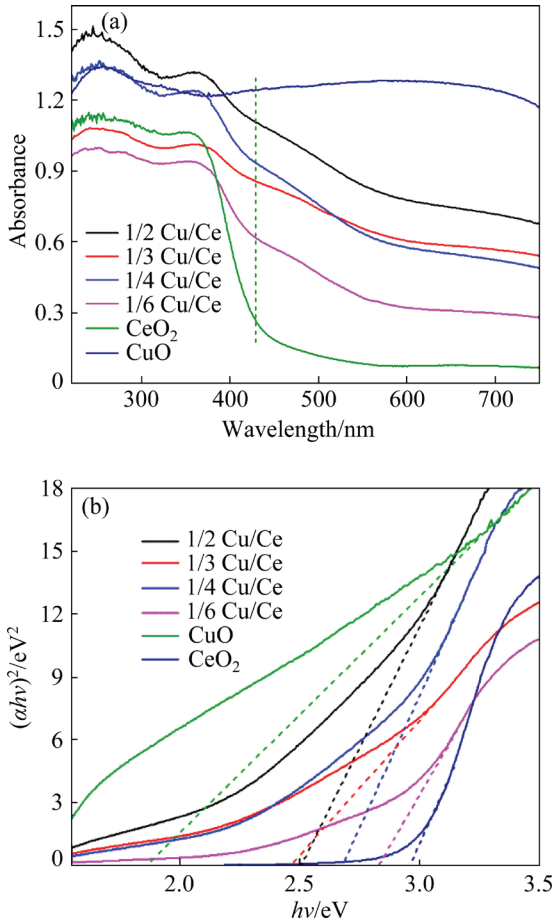

Fig. 5 UV−Vis DRS (a), and $(\alpha hv)^2$−photon energy (hv) relationship curves (b) of CeO_2, CuO and CuO/CeO_2 composites

of CuO regulates the bandgap of the sample, enhancing its light absorption capacity. Furthermore, a shoulder peak was observed at a wavelength of ~430 nm, indicating a defect energy level. The shoulder peak of the CuO/CeO_2 composites broadened and intensified after the introduction of CuO, indicating that the addition of CuO increased the defect concentration in the CuO/CeO_2 composites [35]. The increase in defect concentration is beneficial to promoting the separation of photogenerated electron–hole pairs, thereby improving the photocatalytic activity of the sample.

UV−Vis DRS can be used to estimate the bandgap (E_g) of a sample as follows: $(\alpha hv)^2 = A(hv-E_g)$, where α represents the absorption coefficient; A and hv represent absorption constant and incident photon energy, respectively. Figure 5(b) shows the $(\alpha hv)^2$–photon energy (hv) relationship curves of the prepared samples. The bandgaps of pure CeO_2, CuO, 1/2 Cu/Ce, 1/3 Cu/Ce, 1/4 Cu/Ce, and 1/6Cu/Ce can be obtained via extrapolating the linear part of the curves and are measured to be 2.95, 1.85, 2.51, 2.46, 2.67, and 2.82 eV, respectively. The bandgap of CuO/CeO_2 composites is smaller than that of pure CeO_2, and the decrease in bandgap can be attributed to the formation of a heterojunction composite [36].

Figure 6 shows the obtained PL emission spectra. The PL emission intensity is related to the recombination of photogenerated electrons and holes [37,38]. In general, a higher PL strength indicates rapid electron–hole recombination, while a lower PL strength indicates the inhibition of electron–hole recombination, implying a longer photoelectron lifetime and improved photocatalytic activity. The emission peaks of CuO/CeO_2 composites and CeO_2 samples were observed at 380−550 nm with an excitation wavelength of 243 nm. The prepared CuO/CeO_2 composites exhibited a distinct decrease in emission intensity relative to pure CeO_2, indicating that electron–hole pair recombination was effectively inhibited. This may be attributed to charge transfer between CeO_2 and CuO, which accelerates the carrier migration [39,40]. The 1/3 Cu/Ce sample exhibited the lowest PL intensity, indicating that heterojunction formation considerably enhanced the separation efficiency of photoelectron–hole pairs, prolonging the lifetime of photogenerated electrons and improving the photocatalytic activity of the sample.

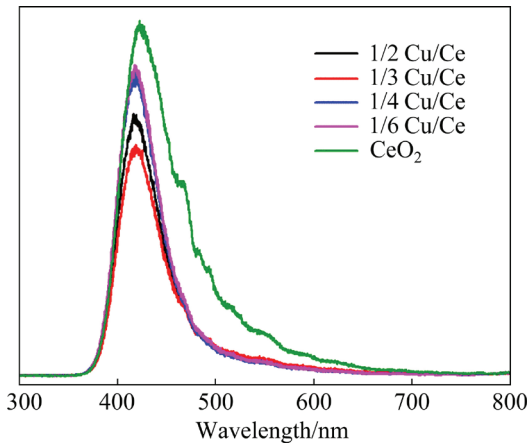

Fig. 6 PL spectra of pure CeO_2 and CuO/CeO_2 composites

Furthermore, the emission spectra of the CuO/CeO_2 composites exhibited a slight blue shift compared to that of pure CeO_2, which may be

attributed to the shift of impurity energy level between Ce (4f) and O (2p) due to the combination of Cu [41]. These results suggest that the CuO/CeO_2 composites can achieve efficient charge transfer and separation between CuO and CeO_2, improving their photocatalytic activity.

The chemical state and elemental composition of pure CeO_2, 1/2 Cu/Ce, 1/3 Cu/Ce, and 1/6 Cu/Ce were further investigated via XPS. For the 1/3 Cu/Ce sample, only the peaks of Ce, Cu, and O were observed in the XPS survey scanning spectrum, indicating that there are no other impurities in the prepared samples (Fig. 7(a)). The Ce 3d orbits were divided into two groups caused by spin-orbit coupling and fitted with eight peaks (Fig. 7(b)). The six peaks labeled u, u″, u‴, v, v″ and v‴ were attributed to the $3d_{3/2}$ and $3d_{5/2}$ for Ce^{4+} states, respectively, and the two peaks labeled u′ and v′ corresponded to the $3d_{3/2}$ and $3d_{5/2}$ for Ce^{3+} states, respectively. This result reveals that Ce^{4+} and Ce^{3+} coexist on the CuO/CeO_2 sample surface. Furthermore, the binding energy of CeO_2 in all CuO/CeO_2 composites was slightly greater than that of pure CeO_2. The shift of the peak position to the high-energy region in the XPS spectrum was due to the reduction of the local electron cloud density [42], confirming that charge transfer occurs at the interface between CuO and CeO_2; this charge transfer changes the chemical environment of Ce^{4+} ions. Based on the peak areas, the Ce^{3+} contents were calculated according to Ref. [43]. The results revealed that the Ce^{3+} contents (mass fraction) in pure CeO_2, 1/2 Cu/Ce, 1/3 Cu/Ce, and 1/6 Cu/Ce were 15.2%, 20.7%, 27.4%, and 16.4%, respectively. A higher Ce^{3+} content indicated a higher content of surface oxygen vacancies, which considerably improved the photocatalytic activity of the nanoparticles [32]. The content of Ce^{3+} ions initially increased and then decreased. The Ce^{3+} content in the 1/3 Cu/Ce sample was the highest. Moreover, the 1/3 Cu/Ce sample exhibited the optimal photocatalytic activity, indicating that a high content of oxygen vacancies plays a leading role in the photocatalytic reaction. This result is also consistent with the results reported in a previous study [44].

Figure 7(c) shows the Cu 2p core-level XPS spectra of 1/2 Cu/Ce, 1/3 Cu/Ce, and 1/6 Cu/Ce.

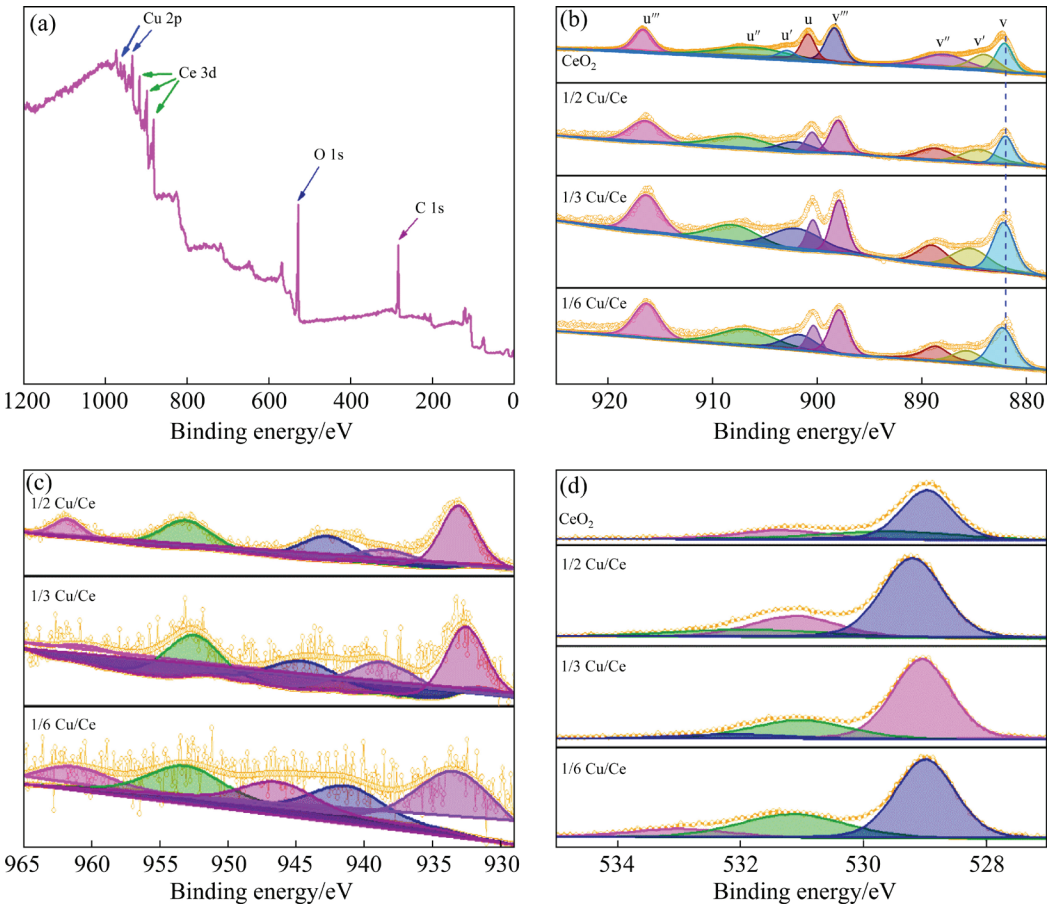

Fig. 7 Wide scanning XPS spectra of 1/3 Cu/Ce (a), XPS spectra of Ce 3d (b), Cu 2p (c), and O 1s (d)

Each sample exhibited two characteristic peaks with a spin-orbit splitting energy gap of 20 eV. The binding energies were located at 933.1, 953.1, 932.7, 952.7, 933.1, and 953.1 eV, in which the binding energies located at 933.1, 932.7 and 933.1 eV were corresponded to the typical characteristic peaks of Cu $2p_{3/2}$ of $Cu^{2+}$and others were assigned to Cu $2p_{1/2}$ of Cu^{2+} [45]. Moreover, there are two satellite peaks near 938−946 eV, which are typical vibration peaks of Cu^{2+} [46]. These results suggested that Cu species in the composites exist mainly as Cu^{2+}, which is consistent with the XRD results.

Figure 7(d) presents the XPS spectra of O 1s of the 1/2 Cu/Ce, 1/3 Cu/Ce, 1/6 Cu/Ce, and pure CeO_2 samples; the O 1s core-level spectrum for all the samples exhibited three peaks. The binding energies of O 1s in 1/3 Cu/Ce composites were observed at 529.0, 531.0, and 532.1 eV. The peaks at 529.0 and 531.0 eV corresponded to lattice oxygen, and the peak at 532.1 eV was attributed to chemisorbed oxygen on the sample surface [47].

3.3 Photocatalytic activity

The photocatalytic performance of the CuO/CeO_2 composites was evaluated through MB degradation experiment under UV irradiation. As shown in Fig. 8, the absorbance of MB gradually decreased with increasing illumination time. The photocatalytic activities of all the CuO/CeO_2 composites were considerably higher than that of pure CeO_2. The photocatalytic activity initially increased and then substantially decreased with increasing CuO content (Fig. 9(a)). After 180 min of illumination, the 1/3 Cu/Ce sample exhibited the highest degradation efficiency of 96.2%, while the pure CeO_2, 1/2 Cu/Ce, 1/4 Cu/Ce, and 1/6 Cu/Ce samples exhibited degradation efficiencies of 78.4%, 80.4%, 92.4%, and 85.8%, respectively. The degradation efficiency of the 1/4 Cu/Ce and 1/6 Cu/Ce samples decreased because of the lower CuO content. Moreover, the number of effective heterojunctions produced via the combination of CuO and CeO_2 was considerably reduced, which in turn decreased the photocatalytic activity. The

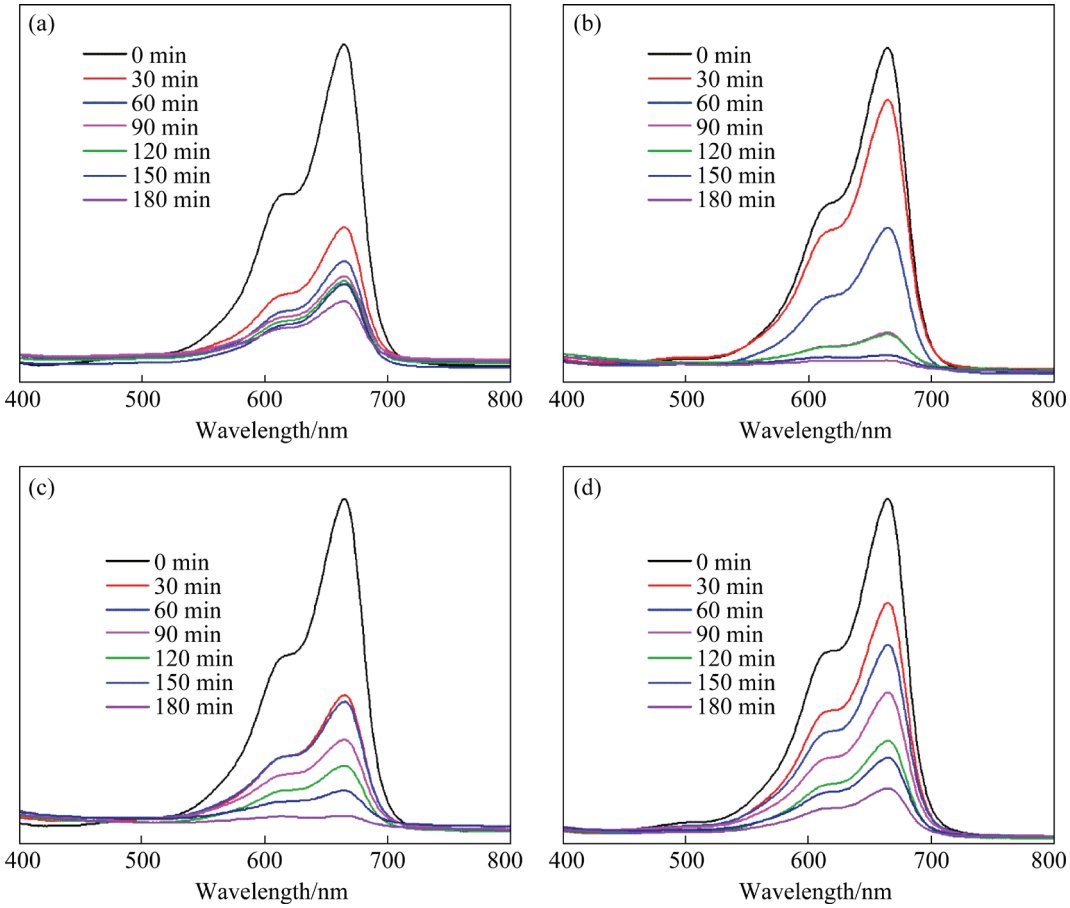

Fig. 8 UV−Vis absorption spectra of MB solution by 1/2 Cu/Ce (a), 1/3 Cu/Ce (b), 1/4 Cu/Ce (c) and 1/6 Cu/Ce (d) composites at different illumination time

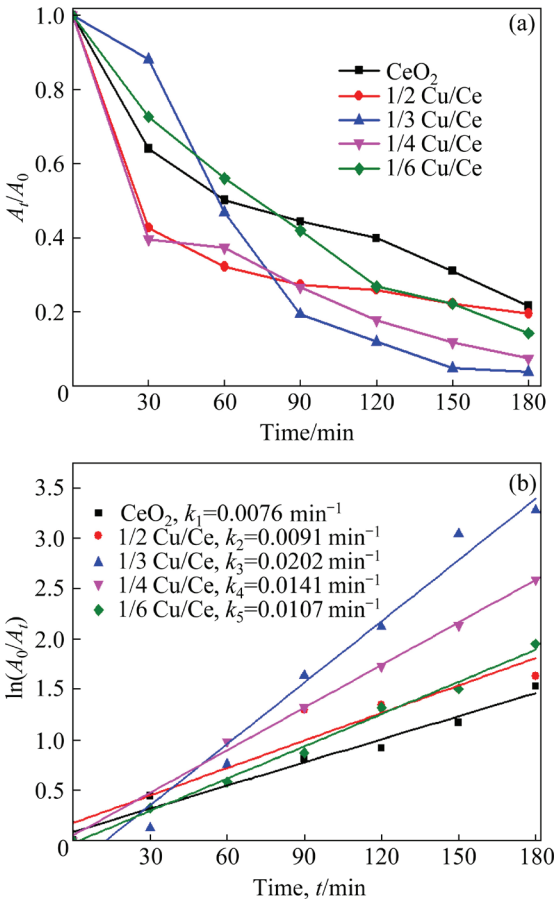

Fig. 9 Photocatalytic degradation curves of MB by CeO_2 and CuO/CeO_2 composites (a), and corresponding pseudo-first-order kinetic curves (b) (k_1–k_5 are pseudo-first-order rate constant for MB degradation)

degradation efficiency of the 1/2 Cu/Ce sample was also lower than that of the 1/3 Cu/Ce sample because the CuO content in the 1/2 Cu/Ce sample was larger than that in the 1/3 Cu/Ce sample. This result can be attributed to the fact that excessive CuO either covers CeO_2 or aggregates itself and no effective heterojunction is formed. Additionally, the bandgap of CuO was small and the photogenerated electron–hole pairs easily recombined, reducing the photocatalytic performance. WANG et al [48] prepared a p-CuO/n-CeO_2 heterojunction photocatalyst. With the addition of H_2O_2, a photocatalytic degradation efficiency of 86.2% was achieved for RhB. Conversely, a photocatalytic degradation efficiency of 96.2% was achieved for the p–n heterojunction CuO/CeO_2 prepared in this study without the addition of H_2O_2.

The pseudo-first-order kinetic curve was obtained via a linear fit of ln (A_0/A_t) and irradiation time (t), as shown in Fig. 9(b). The fitting results of the curve revealed that the photocatalytic degradation process of the MB solution using the prepared sample conforms to the pseudo-first-order kinetic model. As shown in Fig. 9(b), the MB degradation rate of the 1/3 Cu/Ce sample was ~2.7 times that of pure CeO_2. The improved photocatalytic efficiency can be attributed to the formation of p–n-type heterojunctions that promote the rapid transfer of electrons at the CuO/CeO_2 interface and reduce electron–hole recombination.

To study the active species of CuO/CeO_2 composites in the degradation of MB solution, EDTA-2Na, BQ, and TBA were added as h^+, $\cdot O_2^-$, and ·OH scavengers, respectively [49]. Figure 10 shows the photocatalytic efficiency of 1/3 Cu/Ce samples in the presence of various scavengers. With the addition of EDTA-2Na and TBA, the degradation efficiency of MB in the 1/3 Cu/Ce sample decreased, indicating that h^+ and ·OH were involved in the photocatalytic degradation process. However, the photocatalytic efficiency considerably decreased after the addition of BQ, indicating that $\cdot O_2^-$ was the main active species in the degradation process.

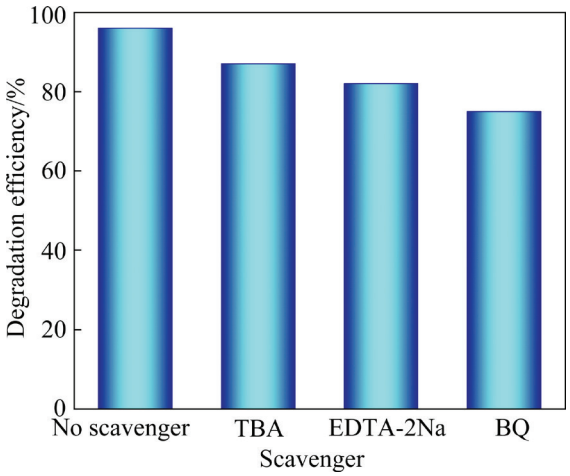

Fig. 10 Scavenger experiment results for photocatalytic degradation of MB by 1/3 Cu/Ce composite

The mechanism of enhanced photocatalytic activity of CuO/CeO_2 composite may be due to the formation of p–n heterojunction between CuO and CeO_2; the diagram of the possible mechanism is shown in Fig. 11. CeO_2 is an n-type semiconductor while CuO is a p-type semiconductor, and their Fermi levels are close to their conduction and

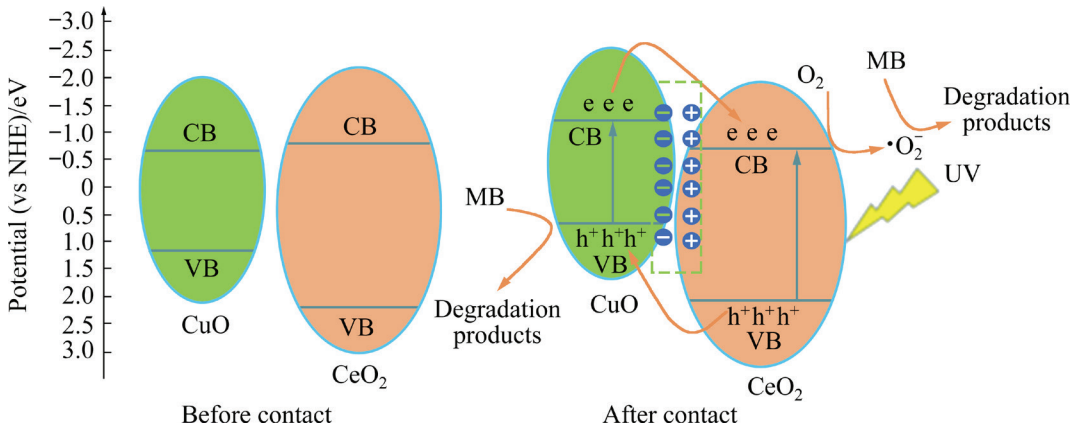

Fig. 11 Possible mechanism of improving photocatalytic activity of CuO/CeO_2 composites

valence bands, respectively. Thus, the Fermi level of CeO_2 is higher than that of CuO. When CuO and CeO_2 are in close contact to form a heterojunction structure, the Fermi energy levels at the interface tend to balance. To achieve this equilibrium, electrons transfer from CeO_2 to CuO through the interface, forming a built-in electric field from n-type CeO_2 to p-type CuO at the semiconductor interface, and at the same time, the Fermi level in the system reaches equilibrium. At this time, the conduction band potential of CuO is more negative than that of CeO_2. The electrons in the CuO conduction band can be rapidly transferred to the conduction band of CeO_2 based on the difference in energy band potential and the action of the built-in electric field. Electrons in the conduction band of CeO_2 can react with O_2 in the MB solution to generate $\cdot O_2^-$, and the $\cdot O_2^-$ formed can effectively degrade the organic pollutant MB. This is consistent with the results of free-radical-trapping experiments.

To further verify the aforementioned mechanism, the method proposed by KRAUT et al [50] was used to calculate the valence band offset (ΔE_{VBO}) and conduction band offset (ΔE_{CBO}) of the CuO/CeO_2 heterostructure. The specific calculation formula is as follows:

$$\Delta E_{VBO} = (E_{Cu,2p} - E_{VB,Cu})_{pure}^{CuO} - (E_{Ce,3d} - E_{VB,Ce})_{pure}^{CeO_2} + \Delta E_{CL} \quad (1)$$

$$\Delta E_{CL} = (E_{Ce,3d} - E_{Cu,2p})_{heterojunction}^{CuO/CeO_2} \quad (2)$$

$$\Delta E_{CBO} = E_g^{CeO_2} - E_g^{CuO} - \Delta E_{VBO} \quad (3)$$

where ΔE_{CL} represents the energy difference between the core energy levels of Cu 2p and Ce 3d in the CuO/CeO_2 heterojunction; $E_{Ce,3d}$ and $E_{Cu,2p}$ represent the core-level binding energies of Ce and Cu elements in CeO_2 and CuO, respectively. $E_{VB,Ce}$ and $E_{VB,Cu}$, and $E_g^{CeO_2}$ and E_g^{CuO} represent the valence band and bandgap of CeO_2 and CuO, respectively. As shown in Figs. 12(a−c), the valence band tops (VBM) of CeO_2 and CuO were 2.22 and 1.18 eV, respectively. The differences between the core energy level and the valence band top of Ce and Cu elements in CeO_2 and CuO were 879.84 and 931.94 eV, respectively.

The difference between the core energy levels of Ce and Cu in the CuO/CeO_2 heterostructure was 50.52 eV. Table 2 lists the core energy levels, valence bands, and bandgaps of CeO_2, CuO, and CuO/CeO_2 heterostructure. According to Eqs. (1)−(3), the ΔE_{VBO} and ΔE_{CBO} values in the CuO/CeO_2 heterostructure were calculated to be 1.58 and −0.48 eV, respectively. ΔE_{CBO} is the main driving force of photoelectron transfer from CuO to CeO_2. A higher conduction band offset indicates a greater driving force for charge separation and transfer. Additionally, ΔE_{VBO} is the primary driving force for transferring photogenerated holes from CeO_2 to CuO. According to the abovementioned equation, ΔE_{VBO} is positive and ΔE_{CBO} is negative, indicating that the valence band and conduction band of CeO_2 are lower than those of CuO. According to the calculation results, the energy band shift diagram of the CuO/CeO_2 heterostructure was constructed, as shown in Fig. 12(d). The calculation results of energy band offset confirm the formation of a p–n heterojunction structure between CuO and CeO_2.

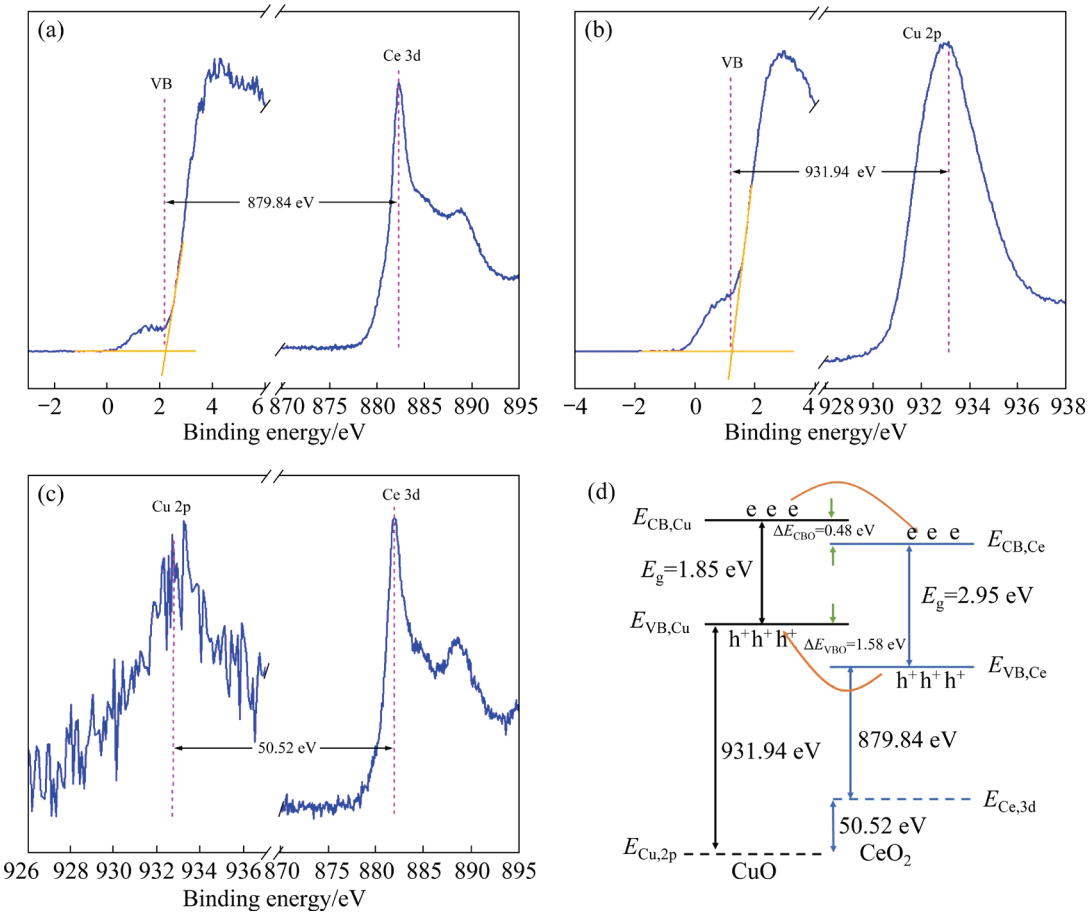

Fig. 12 XPS core energy level and valence band position diagrams for CeO_2 (a), CuO (b), and CuO/CeO_2 (c), and CuO/CeO_2 heterojunction energy band offset diagram (d)

Table 2 XPS binding energies of core levels, VBM and bandgaps for CeO_2, CuO and CuO/CeO_2 heterostructure

Sample	State	Binding energy/eV	E_g/eV
CeO_2	Ce $3d_{5/2}$	882.06	2.95
	VBM	2.22	
CuO	Cu $2p_{3/2}$	933.12	1.85
	VBM	1.18	
CuO/CeO_2	Ce $3d_{5/2}$	882.18	
	Cu $2p_{3/2}$	932.70	

4 Conclusions

(1) The photocatalytic activity of CuO/CeO_2 heterojunction composites for MB was found to be considerably higher than that of CeO_2. The 1/3 Cu/Ce composite exhibited the highest catalytic activity, achieving a degradation efficiency of 96.2% within 180 min.

(2) The p–n heterojunction formed by CuO and CeO_2 can be used to construct an effective electron transport channel, which is beneficial to the efficient separation and rapid transport of photogenerated carriers that considerably improves the photocatalytic performance of the composites.

(3) The band offset of the CuO/CeO_2 heterostructure was calculated; the ΔE_{VBO} and ΔE_{CBO} were 1.58 and −0.48 eV, respectively, demonstrating the formation of a p–n heterojunction.

CRediT authorship contribution statement

Huan-huan CHEN: Conceptualization, Writing − Original draft, Formal analysis; **Shao-hua LUO:** Resources, Writing − Review & editing, Supervision; **Xue-fei LEI:** Writing − Review & editing; **Fei TENG:** Investigation; **Xian-bing JI:** Investigation, Methodology; **Xiao-dong LI:** Supervision.

Declaration of competing interest

The authors declare that they have no known competing financial interests or personal relationships that could have appeared to influence the work reported in this paper.

Acknowledgments

This work was financially supported by the National Natural Science Foundation of China (Nos. 52274295, 52104291, 51874079), the Natural Science Foundation of Hebei Province, China (Nos. E2022501028, E2022501029, E2021501029, A2021501007, E2018501091, E2020501001, E2022501030), the Hebei Province Key Research and Development Plan Project, China (No. 19211302D), Performance Subsidy Fund for Key Laboratory of Dielectric and Electrolyte Functional Material Hebei Province, China (No. 22567627H), the Fundamental Research Funds for the Central Universities, China (Nos. N2223009, N2223010, N2123035, N2023040), the Science and Technology Project of Hebei Education Department, China (No. ZD2022158), and the Central Guided Local Science and Technology Development Fund Project of Hebei Province, China (No. 226Z4401G). The authors would like to thank Xiao-li FAN from Shiyanjia Laboratory for the XPS analysis.

References

[1] QU Jun-nan, SUN Xin-yue, YANG Cheng-lin, XUE Lu, LI Zhong-fu, CUI Bao-long, HU Ying-yue, DU Yi, JI Pei-hong. Novel p−n type polyimide aerogels/BiOBr heterojunction for visible light activated high efficient photocatalytic degradation of organic contaminants [J]. Journal of Alloys and Compounds, 2022, 900: 163469.

[2] XIA Qing, HE Shi-yao, ZHANG Wei, XIANG Qing-chun, QU Ying-dong, REN Ying-lei, QIU Ke-qiang. Degradation efficiency of $Mg_{65}Cu_{25-x}Ag_xY_{10}$ nanoporous dealloyed ribbons on pesticide wastewater [J]. Transactions of Nonferrous Metals Society of China, 2022, 32: 1472−1484.

[3] LU Xiao-xiao, WANG Li-jie, LI Qiang, LUO Rui, ZHANG Jin-feng, TIAN Zhen-fei. Construction of $CoTiO_3$/BiOI p−n heterojunction with nanosheets-on microrods structure for enhanced photocatalytic degradation of organic pollutions [J]. Advanced Powder Technology, 2022, 33: 103354.

[4] PATIL S S, LEE J, KIM T, NAGAPPAGARI L R, LEE K. Controlled synthesis and structural modulation to boost intrinsic photocatalytic activity of $BiVO_4$ [J]. CrystEngComm, 2022, 24: 2686−2696.

[5] FU Si-mei, LI Gang-sen, WEN Xing, FAN Cai-mei, LIU Jian-xin, ZHANG Xiao-chao, LI Rui. Effect of calcination temperature on microstructure and photocatalytic activity of BiOX (X=Cl, Br) [J]. Transactions of Nonferrous Metals Society of China, 2020, 30: 765−773.

[6] JIANG Tao, CHENG Ling, HAN Ying-chun, FENG Jun, ZHANG Jing-dong. One-pot hydrothermal synthesis of Bi_2O_3−WO_3 p−n heterojunction film for photoelectron-catalytic degradation of norfloxacin [J]. Separation and Purification Technology, 2020, 238: 116428.

[7] XIE Li-hao, LU Ding-ze, KONDAMAREDDY K K, HO W, WU Qiong, ZENG Yi-mei, ZHANG Yu-hao, WANG Zhen-nan, ZHAO Bang, LI Jing, YANG Tong-tong, YANG Ning, FAN Hui-qing, LI Lian-bi. Interfacial optimization of oxygen−vacancy-induced 1D/2D CeO_2 nanotubes/g-C_3N_4 step-scheme heterojunction with enhanced visible-light photocatalysis and mechanism insight [J]. Journal of Alloys and Compounds, 2022, 923: 166330.

[8] LIU Guo-long, HOU Guo-yu, XU Mao, QI Xing-yue, SONG Yu-bao, MA Xin-xia, WU Jiang, LUO Guang-qian, YAO Hong, LIU Qi-zhen. Rational design of CeO_2/$Bi_7O_9I_3$ flower-like nanosphere with Z-scheme heterojunction and oxygen vacancy for enhancing photocatalytic activity [J]. Chemical Engineering Journal, 2022, 431: 133254.

[9] WANG Jia-jia, TANG Lin, ZENG Guang-ming, ZHOU Yao-yu, DENG Yao-cheng, FAN Chang-zheng, GONG Ji-lai, LIU Ya-ni. Effect of bismuth tungstate with different hierarchical architectures on photocatalytic degradation of norfloxacin under visible light [J]. Transactions of Nonferrous Metals Society of China, 2017, 27: 1794−1803.

[10] MITTAL M, GUPTA A, PANDEY O P. Role of oxygen vacancies in Ag/Au doped CeO_2 nanoparticles for fast photocatalysis [J]. Solar Energy, 2018, 165: 206−216.

[11] LUO Jin, CHEN Jia-yi, CHEN Xiao-ting, NING Xiao-mei, LIANG Zhan, ZHOU Xiao-song. Construction of cerium oxide nanoparticles immobilized on the surface of zinc vanadate nanoflowers for accelerated photocatalytic degradation of tetracycline under visible light irradiation [J]. Journal of Colloid and Interface Science, 2021, 587: 831−844.

[12] WU Dan-ping, ZHANG Xian, LIU Shi-wen, REN Zi-ying, XING Yong-lei, JIN Xiao-yong, NI Gang. Fabrication of a Z-scheme CeO_2/Bi_2O_4 heterojunction photocatalyst with superior visible-light responsive photocatalytic performance [J]. Journal of Alloys and Compounds, 2022, 909: 164671.

[13] SUN Chun, WANG Yin-ke, WU Li-xu, HU Jun, LONG Xin-qi, WU Hong-tao, JIAO Fei-peng. In situ preparation of novel p–n junction photocatalyst MgAl−LDH/$(BiO)_2CO_3$ for enhanced photocatalytic degradation of tetracycline [J]. Materials Science in Semiconductor Processing, 2022, 150: 106939.

[14] SHI Huan-xian, FAN Jun, ZHAO Yan-yan, HU Xiao-yun, ZHANG Xu, TANG Zhi-shu. Visible light driven $CuBi_2O_4$/Bi_2MoO_6 p−n heterojunction with enhanced photocatalytic inactivation of *E. coli* and mechanism insight [J]. Journal of Hazardous Materials, 2020, 381: 121006.

[15] PENG Yin, YAN Mei, CHEN Qing-guo, FAN Cong-min, ZHOU Hai-yan, XU An-wu. Novel one-dimensional Bi_2O_3−Bi_2WO_6 p−n hierarchical heterojunction with enhanced photocatalytic activity [J]. Journal of Materials Chemistry A, 2014, 22: 8517−8524.

[16] HE Wei, LIU Liang, MA Ting-ting, HAN Hui-min, ZHU Jia-jing, LIU Ying-pei, FANG Zheng, YANG Zhao, GUO Kai. Controllable morphology $CoFe_2O_4$/g-C_3N_4 p-n heterojunction photocatalysts with built-in electric field enhance photocatalytic performance [J]. Applied Catalysis B: Environmental, 2022, 306: 121107.

[17] CHEN Ting-zhen, YANG Cheng-wu, RAJENDRAN S, SAWANGPHRUK M, ZHANG Xin-yu, QIN Jia-qian. Utilizing the built-in electric field of p−n heterojunction to

spatially separate the photogenerated charges in C, N Co-doped Co_3O_4/CdS photocatalysts [J]. Fuel, 2023, 331: 125594.

[18] SONG Hong-bo, WU Rui-yang, YANG Jun-feng, DONG Jian-chao, JI Gui-juan. Fabrication of CeO_2 nanoparticles decorated three-dimensional flower-like BiOI composites to build p−n heterojunction with highly enhanced visible-light photocatalytic performance [J]. Journal of Colloid and Interface Science, 2018, 512: 325−334.

[19] WEN Xiao-ju, NIU Cheng-gang, RUAN Min, ZHANG Lei, ZENG Guang-ming. AgI nanoparticles-decorated CeO_2 microsheets photocatalyst for the degradation of organic dye and tetracycline under visible-light irradiation [J]. Journal of Colloid and Interface Science, 2017, 497: 368−377.

[20] RAJENDRAN S, HOANG T K A, TRUDEAU M L, JALIL A A, NAUSHAD M, AWUAL M R. Generation of novel n−p−n (CeO_2−PPy−ZnO) heterojunction for photocatalytic degradation of micro-organic pollutants [J]. Environmental Pollution, 2022, 292: 118375.

[21] SHEN Chun-hui, WEN Xiao-ju, FEI Zheng-hao, LIU Zong-tang, MU Qi-ming. Visible-light-driven activation of peroxymonosulfate for accelerating ciprofloxacin degradation using CeO_2/Co_3O_4 p−n heterojunction photocatalysts [J]. Chemical Engineering Journal, 2020, 391: 123612.

[22] GNANASEKARAN L, JALIL A A, KUMAR S, RAJENDRAN S, GRACIA F, SOTO-MOSCOSO M, HABILA M A, SARAVANAKUMAR K. Nanoflower shaped NiO/CeO_2 p−n junction material for the degradation of pollutant under visible light [J]. Materials Letters, 2022, 317: 132122.

[23] SABZEHMEIDANI M M, KARIMI H, GHAEDI M. Visible light-induced photo-degradation of methylene blue by n-p heterojunction CeO_2/CuS composite based on ribbon-like CeO_2 nanofibers via electrospinning [J]. Polyhedron, 2019, 170: 160−171.

[24] BHARATHI P, HARISH S, ARCHANA J, NAVANEETHAN M, PONNUSAMY S, MUTHAMIZHCHELVAN C, SHIMOMURA M, HAYAKAWA Y. Enhanced charge transfer and separation of hierarchical CuO/ZnO composites: The synergistic effect of photocatalysis for the mineralization of organic pollutant in water [J]. Applied Surface Science, 2019, 484: 884−891.

[25] DURSUN S, KOYUNCU S N, KAYA I C, KAYA G G, KALEM V, AKYILDIZ H. Production of CuO−WO_3 hybrids and their dye removal capacity/performance from wastewater by adsorption/photocatalysis [J]. Journal of Water Process Engineering, 2020, 36: 101390.

[26] CHEN Huan-huan, LUO Shao-hua, LEI Xue-fei, LIU Huan, LIU Ying-ying, XU Xiao-yu, JIANG Ze-hua, LI Xiao-dong. Synthesis and photocatalytic performance of nano-CeO_2 by a PVP-assisted microwave interface method for organic dye degradation [J]. Ionics, 2020, 26: 5829−5839.

[27] LI Zhen-dong, LIU Dong-fang, ZHAO Ying-xin, LI Song-rong, WEI Xiao-cheng, MENG Fan-sheng, HUANG Wen-li, LEI Zhong-fang. Singlet oxygen dominated peroxymonosulfate activation by CuO−CeO_2 for organic pollutants degradation: Performance and mechanism [J]. Chemosphere, 2019, 233: 549−558.

[28] ZHANG Xiao-long, LI Gui-jing, TIAN Rui-lan, FENG Wen-jie, WEN Lei. Monolithic porous CuO/CeO_2 nanorod composites prepared by dealloying for CO catalytic oxidation [J]. Journal of Alloys and Compounds, 2020, 826: 154149.

[29] CHEN Guo-zhu, XU Qi-hui, YANG Ying, LI Cun-cheng, HUANG Tai-zhong, SUN Guo-xin, ZHANG Shu-xiang, MA Dong-ling, LI Xu. Facile and mild strategy to construct mesoporous CeO_2−CuO nanorods with enhanced catalytic activity toward CO oxidation [J]. ACS Applied Materials & Interfaces, 2015, 7: 23538−23544.

[30] AVGOUROPOULOS G, IOANNIDES T, MATRALIS H. Influence of the preparation method on the performance of CuO−CeO_2 catalysts for the selective oxidation of CO [J]. Applied Catalysis B: Environmental, 2005, 56: 87−93.

[31] MA Xiao-jun, LU Ping, WU Ping. Optical and ferromagnetic properties of hydrothermally synthesized CeO_2/CuO nanocomposites [J]. Ceramics International, 2018, 44: 5284−5290.

[32] CHEN Huan-huan, JIANG Ze-hua, LI Xiao-dong, LEI Xue-fei. Effect of cerium nitrate concentration on morphologies, structure and photocatalytic activities of CeO_2 nanoparticles synthesized by microwave interface method [J]. Materials Letters, 2019, 257: 126666.

[33] HOSSAIN S T, AZEEVA E, ZHANG Ke-fu, ZELL E T, BERNARD D T, BALAZ S, WANG Rui-gang. A comparative study of CO oxidation over Cu−O−Ce solid solutions and CuO/CeO_2 nanorods catalysts [J]. Applied Surface Science, 2018, 455: 132−143.

[34] ZENG Yi-qing, WANG Ya-nan, SONG Fu-jiao, ZHANG Shu-le, ZHONG Qin. The effect of CuO loading on different method prepared CeO_2 catalyst for toluene oxidation [J]. Science of the Total Environment, 2020, 712: 135635.

[35] WANG Min, SHEN Meng, JIN Xi-xiong, TIAN Jian-jian, LI Meng-li, ZHOU Ya-jun, ZHANG Ling-xia, LI Yong-sheng, SHI Jian-lin. Oxygen vacancy generation and stabilization in CeO_{2-x} by Cu-introduction with improved CO_2 photocatalytic reduction activity [J]. ACS Catalysis, 2019, 9: 4573−4581.

[36] YULIZAR Y, GUNLAZUARDI J, APRIANDANU D O B, SYAHFITRI T W W. CuO-modified $CoTiO_3$ via catharanthus roseus extract: A novel nanocomposite with high photocatalytic activity [J]. Materials Letters, 2020, 277: 128349.

[37] WANG An-qi, ZHENG Zhi-keng, WANG Hui, CHEN Yu-wen, LUO Cheng-hui, LIANG Ding-jun, HU Bo-wen, QIU Rong-liang, YAN Kai. 3D hierarchical H_2-reduced Mn-doped CeO_2 microflowers assembled from nanotubes as a high-performance Fenton-like photocatalyst for tetracycline antibiotics degradation [J]. Applied Catalysis B: Environmental, 2020, 277: 119171.

[38] LI Hai-bin, HUANG Guo-you, ZHANG Jian, FU Sheng-hao, WANG Teng-gan, LIAO Hong-wei. Photochemical synthesis and enhanced photocatalytic activity of MnO_x/$BiPO_4$ heterojunction [J]. Transactions of Nonferrous Metals Society of China, 2017, 27: 1127−1133.

[39] HUO Quan, LIU Gong-quan, SUN Hai-hui, FU Yan-fei, NING Yao, ZHANG Bo-yu, ZHANG Xu-biao, GAO Jing, MIAO Jia-run, ZHANG Xiao-lin, LIU Su-yan. CeO_2-

modified MIL-101(Fe) for photocatalysis extraction oxidation desulfurization of model oil under visible light irradiation [J]. Chemical Engineering Journal, 2021, 422: 130036.

[40] ZHANG Xiang-hui, ZHANG Ming-ming, CAO Kai-xuan. Hydrothermal synthesis of Sm-doped Bi_2WO_6 flower-like microspheres for photocatalytic degradation of rhodamine B [J]. CrystEngComm, 2019, 21: 6208−6218.

[41] KUMAR S, AHMED B, SINGH A, SINGH A, OJHA A K. Experimental and theoretical investigations of unusual enhancement of room temperature ferromagnetism in nickel-cobalt codoped CeO_2 nanostructures [J]. Journal of Magnetism and Magnetic Materials, 2018, 465: 756−761.

[42] ZHANG Jian, XIN Jia-yu, SHAO Chang-lu, LI Xing-hua, LI Xiao-wei, LIU Shuai, LIU Yi-chun. Direct Z-scheme heterostructure of *p*-$CuAl_2O_4$/*n*-Bi_2WO_6 composite nanofibers for efficient overall water splitting and photodegradation [J]. Journal of Colloid and Interface Science, 2019, 550: 170−179.

[43] CHEN Shao-qing, LI Li-ping, HU Wan-biao, HUANG Xin-song, LI Qi, XU Yang-sen, ZUO Ying, LI Guang-she. Anchoring high-concentration oxygen vacancies at interfaces of CeO_{2-x}/Cu toward enhanced activity for preferential CO oxidation [J]. ACS Applied Materials & Interfaces, 2015, 7: 22999−23007.

[44] KHAN M M, ANSARI S A, ANSARI M O, MIN B K, LEE J, CHO M H. Biogenic fabrication of Au@CeO_2 nanocomposite with enhanced visible light activity [J]. Journal of Physical Chemistry C, 2014, 118: 9477−9484.

[45] WANG Jing, ZHONG Li-ping, LU Ji-chang, CHEN Ran, LEI Yan-qiu, CHEN Ke-zhen, HAN Cai-yun, HE Su-fang, WAN Geng-ping, LUO Yong-ming. A solvent-free method to rapidly synthesize CuO−CeO_2 catalysts to enhance their CO preferential oxidation: Effects of Cu loading and calcination temperature [J]. Molecular Catalysis, 2017, 443: 241−252.

[46] CÁMARA A L, CORBERÁN V C, MARTÍNEZ-ARIAS A, BARRIO L, SI R, HANSON J C, RODRIGUEZ J A. Novel manganese-promoted inverse CeO_2/CuO catalyst: In situ characterization and activity for the water-gas shift reaction [J]. Catalysis Today, 2020, 339: 24−31.

[47] ALLA S K, DEVARAKONDA K K, KOMARALA E V P, MANDAL R K, PRASAD N K. Ferromagnetic Fe-substituted cerium oxide nanorods: Synthesis and characterization [J]. Materials and Design, 2017, 114: 584−590.

[48] WANG Ning, PAN Ye, LU Tao, LI Xing-zhou, WU Shi-kai, WU Ji-li. A new ribbon-ignition method for fabricating p-CuO/n-CeO_2 heterojunction with enhanced photocatalytic activity [J]. Applied Surface Science, 2017, 403: 699−706.

[49] ZHENG Li-li, XIAO Xin-yan, LI Yang, ZHANG Wei-ping. Enhanced photocatalytic activity of TiO_2 nanoparticles using WS_2/g-C_3N_4 hybrid as co-catalyst [J]. Transactions of Nonferrous Metals Society of China, 2017, 27: 1117–1126.

[50] KRAUT E A, GRANT R W, WALDROP J R, KOWALCZYK S P. Precise determination of the valence-band edge in X-ray photoemission spectra: application to measurement of semiconductor interface potentials [J]. Physical Review Letters, 1980, 44: 1620–1623.

CuO/CeO_2 p−n 异质结光催化降解亚甲基蓝的性能及机理

陈欢欢[1,2]，罗绍华[1,2]，雷雪飞[1,2]，滕 飞[1,2]，纪献兵[3]，李晓东[1]

1. 东北大学 材料科学与工程学院，沈阳 110819；
2. 东北大学 秦皇岛分校 河北省电介质与电解质功能材料重点实验室，秦皇岛 066004；
3. 河北环境工程学院 环境工程系，秦皇岛 066102

摘 要：采用简单微波回流法和均相沉淀技术合成 CuO/CeO_2 p−n 异质结复合材料，并对其光催化降解亚甲基蓝溶液的性能进行研究。CuO/CeO_2 异质结复合材料的降解效率明显强于 CeO_2。结果表明，以 Cu/Ce 摩尔比为 1/3 制备的复合材料(1/3 Cu/Ce)的光催化活性最高，在 180 min 内降解效率达到 96.2%。CuO 和 CeO_2 之间形成的 p−n 异质结促进了光生载流子的分离和传输，从而提高了其光催化活性。计算了 CuO/CeO_2 异质结的能带位置偏移，其价带偏移(ΔE_{VBO})为 1.58 eV，导带偏移(ΔE_{CBO})为−0.48 eV。计算结果进一步证明 CuO 与 CeO_2 之间形成了 p−n 异质结。

关键词：CuO；CeO_2；p−n 异质结；光催化机理；亚甲基蓝

(Edited by Wei-ping CHEN)